Andoh *et al. Earth, Planets and Space* (2023) 75:86
https://doi.org/10.1186/s40623-023-01837-0

Earth, Planets and Space

FULL PAPER

Open Access

Simulation of horizontal sporadic E layer movement driven by atmospheric tides

Satoshi Andoh[1,2*], Akinori Saito[1] and Hiroyuki Shinagawa[3]

Abstract

The present study aims to reveal horizontal sporadic E (Es) movements driven by atmospheric diurnal/semi-diurnal tides using a three-dimensional (3D) ionospheric model. Horizontal Es movements have been investigated since the mid-twentieth century, using a variety of 1D/2D observational techniques. However, there are no comprehensive studies that explain the different results asserted by the observations. Herein, we performed 3D Es simulations at mid- and low-latitudes. This is the first study to investigate horizontal Es movements from a 3D perspective. We found that the Es layers are constrained at the zonal-wind shear nodes above ~110 km, but transported by horizontal winds below ~110 km. The Es layers that descend with the downward tidal phases move southward. The descending Es layers move westward as they lag behind the zonal-wind shear nodes. The Es layers that stagnate at ~100 km are transported by the semi-diurnal tides. In general, the descending and stagnating Es layers do not move eastward. This is because the Es layers diffuse vertically in the eastward/northward wind region or in the early stage of formation in the eastward/southward wind region. The horizontal Es movement tendency in the simulations agreed with and provided a general explanation for previous observations.

Keywords Sporadic E layer, Ionosphere, Simulation, Atmospheric tide, Mid-latitude, Low-latitude, Metal ion

*Correspondence:
Satoshi Andoh
andoh@nict.go.jp
Full list of author information is available at the end of the article

Graphic Abstract

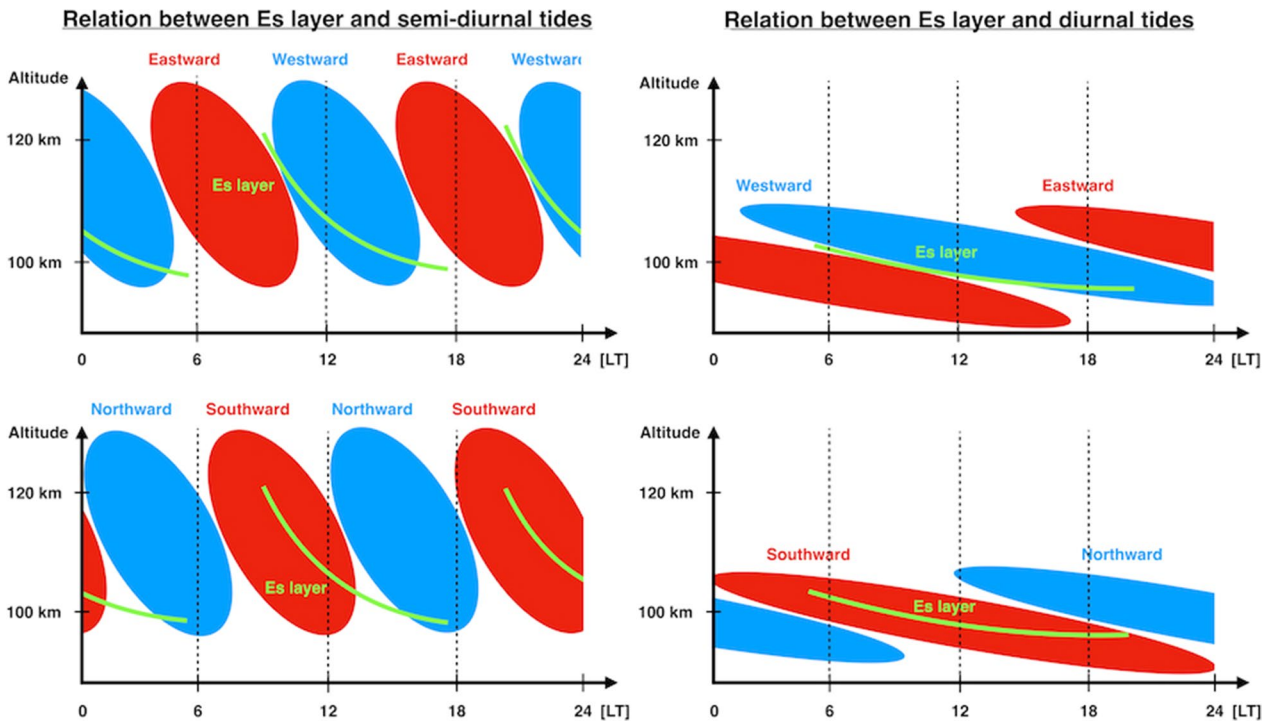

Introduction

Sporadic E (Es) layers are highly dense plasma layering structures that appear in the ionospheric *E* region. The Es layers consist mainly of metal ions (e.g., Mg^+, Fe^+, and Ca^+) and are also known as metal/metallic ion layers (e.g., Huba et al. 2019; Andoh et al. 2021). A variety of observations (e.g., Whitehead 1970, 1989; Mathews 1998; Haldoupis 2012; Raizada et al. 2020; Obenberger et al. 2021; Sun et al. 2021) and simulations (e.g., Mathews and Bekeny 1979; Carter and Forbes 1999; Resende et al. 2016; Andoh et al. 2020, 2022) have been conducted to elucidate temporal and spatial variations in the Es layers.

Wind shear theory is a widely accepted formation mechanism of Es layers at geomagnetic mid-latitudes (Whitehead 1961; Axford 1963). It should be noted that, in this study, we use "geomagnetic" to refer to the latitudes in geomagnetic coordinates, and do not explicitly use "geographic" to refer to the latitudes in geographic coordinates. According to wind shear theory, the vertical shear of horizontal winds drives vertical ion convergence and creates Es layers. The meridional winds above ~130 km and zonal winds below ~130 km control the vertical ion convergence because of the ion–neutral frictional force along the magnetic fields and vertical Lorentz force, respectively. The meridional wind vertical shears that cause Es layer formation are characterized by poleward winds above and equatorward winds below, and those of zonal winds are characterized by westward winds above and eastward winds below. This wind shear theory can explain the vertical Es dynamics. However, this cannot explain the mechanism of horizontal Es movements.

Horizontal Es movements have been investigated extensively at mid- and low-latitudes (Whitehead 1989; Maeda and Heki 2014; Muafiry et al. 2018; Sun et al. 2021, and references therein). In meridional Es movements, some observations have found that the Es layers move with the meridional phases of the semi-diurnal tides (Koizumi 1969; Beynon et al. 1972; Rao and Rao 1972; Tanaka 1979; Maeda and Heki 2015). However, a southward tendency of horizontal Es movements has also been observed (Beynon et al. 1972; Sun et al. 2021). In zonal Es movements, it has been reported that the Es layers move westward rather than eastward (Koizumi 1969; Beynon et al. 1972; Kolawole and Derblom 1978; Tanaka 1979; Sun et al. 2021). However, Beynon et al. (1972) and Tanaka (1979) also observed eastward Es movements, likely owing to semi-diurnal tides. No

physical mechanism has been provided for the different horizontal Es movements. This is probably because the horizontal Es movements have not been discussed in terms of both altitude and local time at which Es layers appear.

Previous studies estimated horizontal Es movements from one-dimensional or two-dimensional observations (e.g., Koizumi 1969; Beynon et al. 1972; Tanaka 1979; Maeda and Heki 2015; Sun et al. 2021). These observations cannot distinguish between the spatial and temporal evolution of the Es layers. Recently, numerical simulations have revealed the three-dimensional (3D) dynamics and distribution of Es layers (Huba et al. 2019; Andoh et al. 2021; Wu et al. 2021). Andoh et al. (2021) showed that horizontal Es movements are crucial for Es layer sporadicity. They also suggested a westward moving tendency of the Es layers. This is because the Es layers lag behind the zonal-wind shear nodes, where the zonal wind velocity is zero, and become embedded in the westward wind regions. However, they did not fully investigate the relationship between atmospheric tides and horizontal Es movements in terms of the Es layer altitude and local time. Moreover, the simulated Es layers at mid-latitudes were formed by semi-diurnal tides and not by diurnal tides. It is well known that diurnal tides also play a key role in the formation of Es layers especially at low-latitudes (Whitehead 1989; Mathews 1998; Haldoupis 2011, 2012). Further 3D investigations are needed to reveal the horizontal Es movements caused by both semi-diurnal and diurnal tides.

As mentioned earlier, horizontal Es movements are considered to be caused by ion transport due to semi-diurnal/diurnal tides (e.g., Tanaka 1979; Maeda and Heki 2015; Sun et al. 2021). Diurnal tides are stronger at low-latitudes than at mid-latitudes (Hagan et al. 1999; Manson et al. 1999; Oberheide et al. 2015). Diurnal tides can propagate up to ~ 110 km at low-latitudes (Hagan and Forbes 2002; Oberheide et al. 2015; Solomon and Roble 2015). Semi-diurnal tides are stronger at mid-latitudes than at low-latitudes (Hagan et al. 1999; Manson et al. 1999; Oberheide et al. 2015). A combination of semi-diurnal and diurnal tides can result in different horizontal Es movements between mid-latitudes and low-latitudes.

Recently, we have performed Es simulations at low- and mid-latitudes (Andoh et al. 2020, 2022). We succeeded in reproducing the day-to-day variations in the observed Es layers formed by diurnal and semi-diurnal tides. In this study, we simulated 3D structures of mid-latitude and low-latitude Es layers. We aimed to reveal how diurnal and semi-diurnal tides drive the horizontal Es movements in terms of the local time and Es layer altitudes, and attempted to provide a general mechanism for horizontal Es movements.

Methods

Model description

We utilized the same numerical, local, ionospheric model employed in Andoh et al. (2022). This model solves the chemical and physical processes of NO^+, O_2^+, O^+, and Mg^+. A detailed description of the ionospheric model is provided in Andoh et al. (2020, 2022). The horizontal domain of the ionospheric model was 20° latitude × 20° longitude with a 0.25° grid spacing. The altitudinal coverage ranged from 85 to ~220 km with a 0.5–2 km grid spacing. The neutral density and temperature were constrained using the NRLMSISE-00 model (Picone et al. 2002). Geomagnetic fields were obtained from the IGRF-12 model (Thébault et al. 2015). The Ap and F10.7 indices for each simulated day were obtained from the World Data Center for Geomagnetism in Kyoto (http://wdc.kugi.kyoto-u.ac.jp/wdc/Sec3.html) and NOAA/NCEI (https://www.ngdc.noaa.gov/stp/spaceweather.html), respectively.

The 3D neutral winds were obtained from the GAIA model (Ground-to-topside model of Atmosphere and Ionosphere for Aeronomy) (Jin et al. 2011, 2012). The atmospheric portion of the GAIA model assimilates weather reanalysis data below 40 km (Jin et al. 2012). Therefore, the GAIA model can reproduce realistic atmospheric waves that propagate from the lower atmosphere to the ionosphere (Miyoshi et al. 2018). In fact, using the neutral winds of the GAIA model, our numerical model succeeded in reproducing the Es layers at mid- and low-latitudes observed by a lidar at Tokyo and the incoherent scatter radar at Arecibo (Andoh et al. 2020, 2022). The GAIA model neutral wind grid spacing is 2.8° longitude, 2.8° latitude, and 0.2 scale height above the tropopause (Miyoshi et al. 2017). The GAIA model neutral winds were interpolated to adapt to the ionospheric model grid spacing. Due to the large grid spacing of the GAIA model, we focused on hundred-kilometer-scale Es layer structures in this study.

To assess the effects of the semi-diurnal and diurnal tides on horizontal Es movements, we investigated low- and mid-latitude Es layers simulated as Andoh et al. (2020, 2022). In both the mid-latitude and low-latitude Es simulations, Mg^+ was used as a proxy for metal ions. To simulate the mid-latitude Es layers, the center of the horizontal numerical domain was set to 35.7°N latitude and 139.4°E longitude (26.9° geomagnetic latitude; 48.9° inclination) around Tokyo, Japan. To simulate the low-latitude Es layers, it was set to 18.3°N latitude and 66.8°W longitude (27.2° geomagnetic latitude;

45.7° inclination) around the Arecibo radar. Both Japan and Arecibo are located in geomagnetic mid-latitude regions.

Variable definitions

We have summarized the definitions of the variables to examine 3D Es layer dynamics caused by atmospheric tides. The ion velocity driven by neutral winds ($\vec{V}_{i,wind}$) was calculated using the following equation:

$$\vec{V}_{i,wind} = \frac{\xi^2}{1+\xi^2}\vec{V}_n + \frac{\xi}{1+\xi^2}(\vec{V}_n \times \vec{b}) + \frac{1}{1+\xi^2}(\vec{V}_n \cdot \vec{b})\,\vec{b}, \quad (1)$$

with

$$\xi = \frac{\nu_{in}}{\Omega_i}, \quad (2)$$

where $\vec{V}_n$ is the neutral wind velocity, $\vec{b}$ is the unit vector of the geomagnetic field, ν_{in} is the ion–neutral collision frequency, and Ω_i is the ion gyro-frequency. The positive direction of $\vec{V}_{i,wind}$ is vertically upward, southward, and eastward. The first, second, and third terms on the right-hand side represent the ion motions together with neutrals, Lorentz forced ion motions, and ion–neutral frictional forced ion motions constrained along the geomagnetic fields, respectively.

We calculated compression and transport effects on ion density variations by winds. Based on the ion continuity equation, ion density variations controlled by winds were defined as:

$$\frac{\partial N_i}{\partial t} = -N_i \nabla \cdot \vec{V}_{i,wind} - \vec{V}_{i,wind} \cdot \nabla N_i. \quad (3)$$

The first and second terms in the right-hand side show density variations by compression and transport, respectively. Comparing those variables, we can investigate which term is effective for Es layer density variations. Es layer dynamics is considered to be controlled primarily by vertical compression, and thus, we need to examine how horizontal transport affects Es layer dynamics compared to vertical compression. Because our ionospheric numerical model used spherical coordinates, the vertical, meridional, and zonal differential flux density (VDFD, MDFD, and ZDFD) of metal ions, that is a summation of compression and transport, were defined as:

$$VDFD = -\frac{1}{r^2}\frac{\partial}{\partial r}(r^2 w_{i,wind} N_i), \quad (4)$$

$$MDFD = -\frac{1}{r\sin\theta}\frac{\partial}{\partial \theta}(\sin\theta v_{i,wind} N_i), \quad (5)$$

$$ZDFD = -\frac{1}{r\sin\theta}\frac{\partial}{\partial \phi}(u_{i,wind} N_i), \quad (6)$$

where r, θ, and ϕ are the radius, colatitude and longitude, respectively. $w_{i,wind}$, $v_{i,wind}$, and $u_{i,wind}$ are the vertical, meridional, and zonal components of $\mathbf{V}_{i,wind}$. The vertical, meridional, and zonal compression (VC, MC, and ZC) of metal ions were defined as:

$$VC = -\frac{N_i}{r^2}\frac{\partial}{\partial r}(r^2 w_{i,wind}), \quad (7)$$

$$MC = -\frac{N_i}{r\sin\theta}\frac{\partial}{\partial \theta}(\sin\theta v_{i,wind}), \quad (8)$$

$$ZC = -\frac{N_i}{r\sin\theta}\frac{\partial}{\partial \phi}(u_{i,wind}). \quad (9)$$

The vertical, meridional, and zonal ion transportation (VT, MT, and ZT) of metal ions were defined as:

$$VT = -w_{i,wind}\frac{\partial N_i}{\partial r}, \quad (10)$$

$$MT = -\frac{v_{i,wind}}{r}\frac{\partial N_i}{\partial \theta}, \quad (11)$$

$$ZT = -\frac{u_{i,wind}}{r\sin\theta}\frac{\partial N_i}{\partial \phi}. \quad (12)$$

The units of the variables in Eqs. 4, 5, 6, 7, 8, 9, 10, 11, 12 are $m^{-3}\ s^{-1}$. The positive values of these nine variables indicate ion density enhancements and vice versa.

Results

Figure 1 displays the temporal variations in (a, d) Mg^+ ion density, (b, e) zonal winds (eastward positive), and (c, f) meridional winds (southward positive). The upper three plots are those at Tokyo, Japan (35.7°N and 139.4°E) on June 3, 2015 (a–c). The three lower plots are those at Arecibo (18.3°N and 66.8°W) on October 20, 1998 (d–f). The locations shown in the upper and lower panels are the numerical domain centers for the mid- and low-latitude cases, respectively. The contours in Fig. 1a and d show the geomagnetic zonal wind velocity. The geomagnetic zonal winds (u_m) are calculated as:

$$u_m = u_n \cos D + v_n \sin D, \quad (13)$$

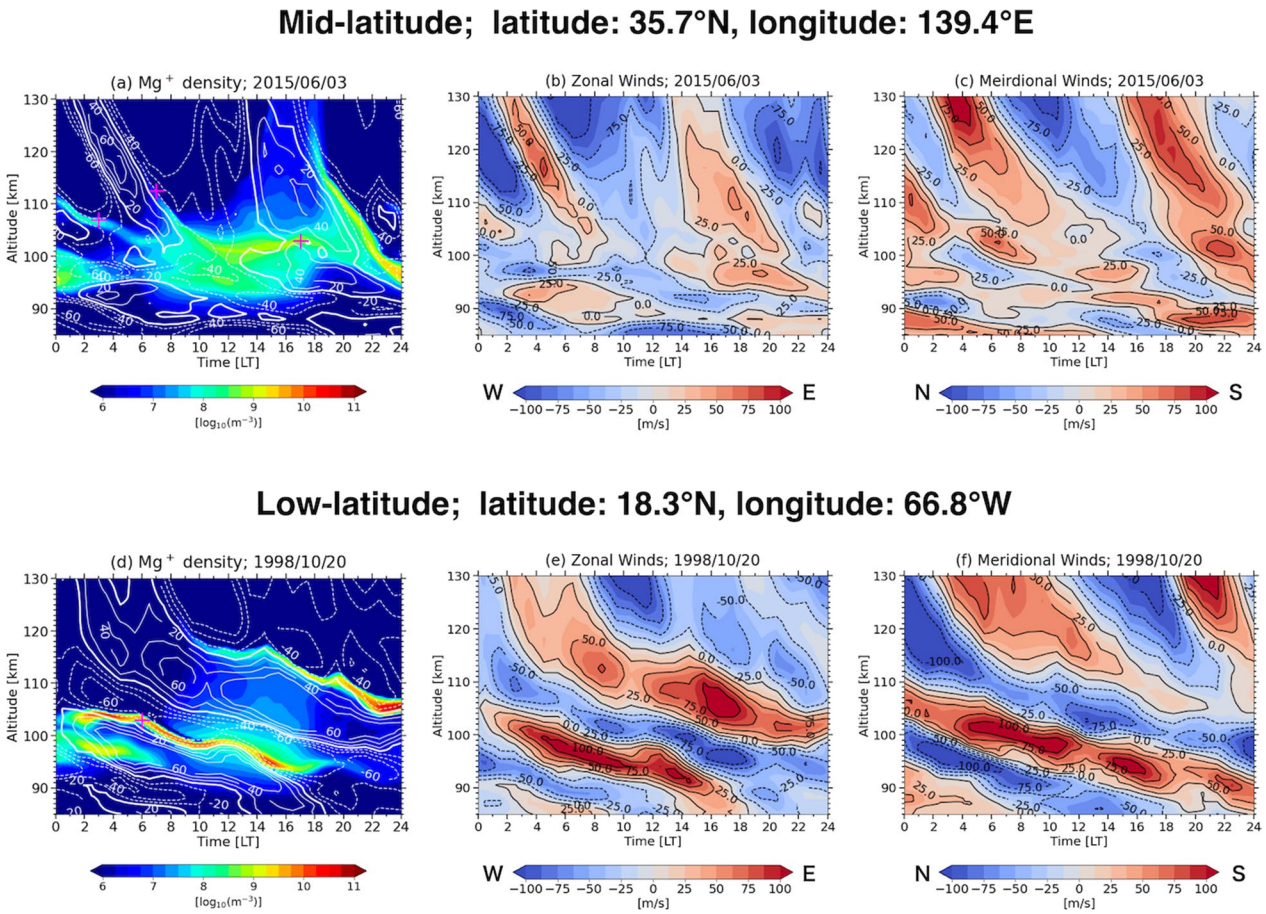

Fig. 1 Temporal variations in **a**, **d** Mg^+ ion density; **b**, **e** zonal winds (eastward positive); and **c**, **f** meridional winds (southward positive). The upper three plots are those at Tokyo, Japan (35.7°N and 139.4°E) on June 3, 2015 (**a**–**c**). The lower three plots are those at Arecibo (18.3°N and 66.8°W) on October 20, 1998 (**d**–**f**). The contours in Fig. 1a and d show the geomagnetic zonal wind velocity. Thick contours represent 0 m/s, and dashed and solid contours represent geomagnetic westward and eastward winds with 20 m/s intervals, respectively. The magenta crosses in subplots a and d indicate the altitudes and local times at which horizontal Es movements were investigated in this study

where D is the geomagnetic field declination, and u_n and v_n are the zonal and meridional winds, respectively. Again, we use "geomagnetic" to refer to geomagnetic coordinate latitudes, and do not use explicitly "geographic" to refer to geographic coordinate latitudes.

We chose the specific two dates because it was obvious that the semi-diurnal tides are dominant at mid-latitudes (Fig. 1b and c) and that the diurnal tides are dominant at low-latitudes (Fig. 1e and f). These are typical characteristics of the mesosphere and lower thermosphere at mid- and low-latitudes (Hagan et al. 1999; Manson et al. 1999; Hagan and Forbes 2002; Oberheide et al. 2015; Solomon and Roble 2015). It is well known that diurnal and semi-diurnal tides are the most crucial tides for Es layer dynamics (Mathews and Bekeny 1979; Whitehead 1989; Mathews 1998; Haldoupis et al. 2006; Haldoupis 2011, 2012). Therefore, on the two days, we could investigate the general horizontal Es layer movements by neutral winds.

In Fig. 1a, the daytime Es layer descends from 115 km at 6 LT to 103 km at 11 LT. It broadens and stagnates at ~103 km between 11 and 18 LT. The nighttime Es layers descend from 110 km and 0 LT to 103 km and 6 LT, and from 125 km at 18 LT to 96 km at 24 LT. The daytime Es layer lags behind the geomagnetic zonal-wind shear nodes, where the geomagnetic zonal wind velocity is zero, especially after 8 LT. This lag is caused by the more frequent ion–neutral collisions that inhibit the vertical ion motions in the lower altitudes. The nighttime Es layers also deviate from the geomagnetic zonal-wind shear nodes. As shown in Fig. 1b and c, the semi-diurnal tides prevail, but the diurnal tides do not at mid-latitudes. The daytime and nighttime Es layers are formed by the semi-diurnal tides. At low-latitudes, the upper Es layer appears

at 120 km and 8 LT and descends to 105 km at 24 LT with the geomagnetic zonal-wind shear nodes. The lower Es layer descends from 105 km at 2 LT to 95 km at 17 LT, as shown in Fig. 1d. It lags slightly behind the geomagnetic zonal-wind shear nodes after 13 LT. As shown in Fig. 1e and f, at low-latitudes, the diurnal tides prevail below ~110 km, and the semi-diurnal tides prevail above ~ 110 km. The lower Es layer is formed by the diurnal tides, and the upper Es layer is formed by both semi-diurnal and diurnal tides.

Hereafter, we examined the horizontal Es movements at mid- and low-latitudes, comparing them to the local wind distributions at the same altitudes and local times. We focused on the semi-diurnal tidal effects at mid-latitudes and the diurnal tidal effects at low-latitudes for horizontal Es movements.

Horizontal Es movements driven by semi-diurnal tides

Figure 2 shows the horizontal distributions at 112.5 km and 7 LT of (a) Mg^+ density, (b) zonal winds (eastward positive), and (c) meridional winds (southward positive) at mid-latitudes around Japan. The altitude and local time correspond to those of the daytime descending Es layer (DEsL) in its early stage, as shown in Fig. 1a, which is denoted by the magenta cross at 7 LT. The contours in Fig. 2a represent the geomagnetic zonal wind velocity. Figure 2a shows that the daytime Es layer forms near the geomagnetic zonal wind shear nodes. The Es layer spreads at 32–43°N and 137–147°E. It occurs near the geomagnetic zonal-wind shear nodes, where the geomagnetic zonal wind velocity is zero. As shown in Fig. 2b and c, around the Es layer, the zonal winds are weak (within ±12.5 m/s), and the meridional winds are nearly 50 m/s southward.

To distinguish the temporal and spatial variations in the Es layers on the horizontal cross-sections, the Es density variation mechanisms were examined from a 3D perspective. Figure 3 displays the horizontal distributions of the variables defined by Eqs. 4, 5, 6, 7, 8, 9, 10, 11, 12 at 112.5 km and 7 LT. The color range is between -4.0×10^4 and 4.0×10^4 m^{-3} s^{-1}. Positive variable values indicate ion density enhancements, and vice versa. The first, second, and third columns show the compression, transportation, and differential flux density, respectively. The first, second, and third rows show density variations due to vertical dynamics (VC, VT, and VDFD), meridional dynamics (MC, MT, and MDFD), and zonal dynamics (ZC, ZT, and ZDFD), respectively. The fourth row shows the total variables displayed in the first, second, and third rows. In the first column, VC is on the order of 10^4 m^{-3} s^{-1}, and MC and ZC is on the order of 10^2 m^{-3} s^{-1}. VC is greater than MC and ZC, as predicted by wind shear theory. The total VC, MC, and ZC are approximately equivalent to VC, as shown in the fourth row of the first column. In the second column, VT is on the order of 10^4 m^{-3} s^{-1}, and MT and ZT are on the order of 10^3 m^{-3} s^{-1} and 10^2 m^{-3} s^{-1}, respectively. VT is greater than MT and ZT because the Es layer has intense vertical density variations, that is, a large $\frac{\partial N_i}{\partial z}$. Consequently, VDFD is greater than MDFD and ZDFD as shown in the third column. The total of these three variables is nearly equal to VDFD. Therefore, the temporal evolution in 3D Es structures above ~110 km are determined primarily by vertical ion dynamics (VC and VT). In other words,

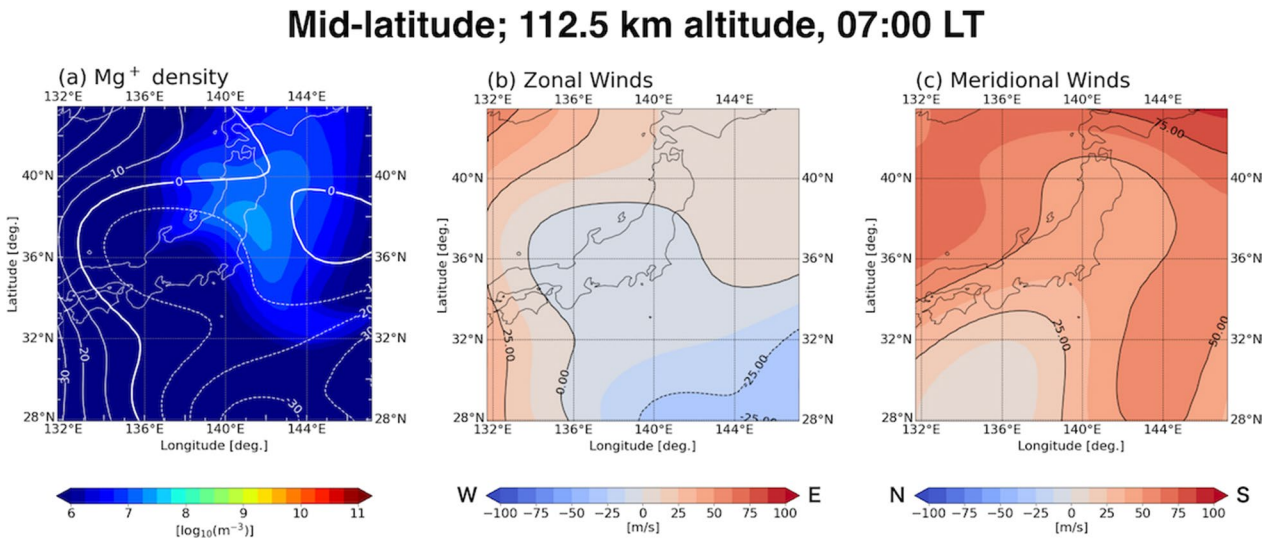

Fig. 2 Horizontal distributions at 112.5 km and 7 LT for **a** Mg^+ density, **b** zonal winds (eastward positive), and **c** meridional winds (southward positive) at mid-latitudes around Japan. The contours in Fig. 2a represent the geomagnetic zonal wind velocity

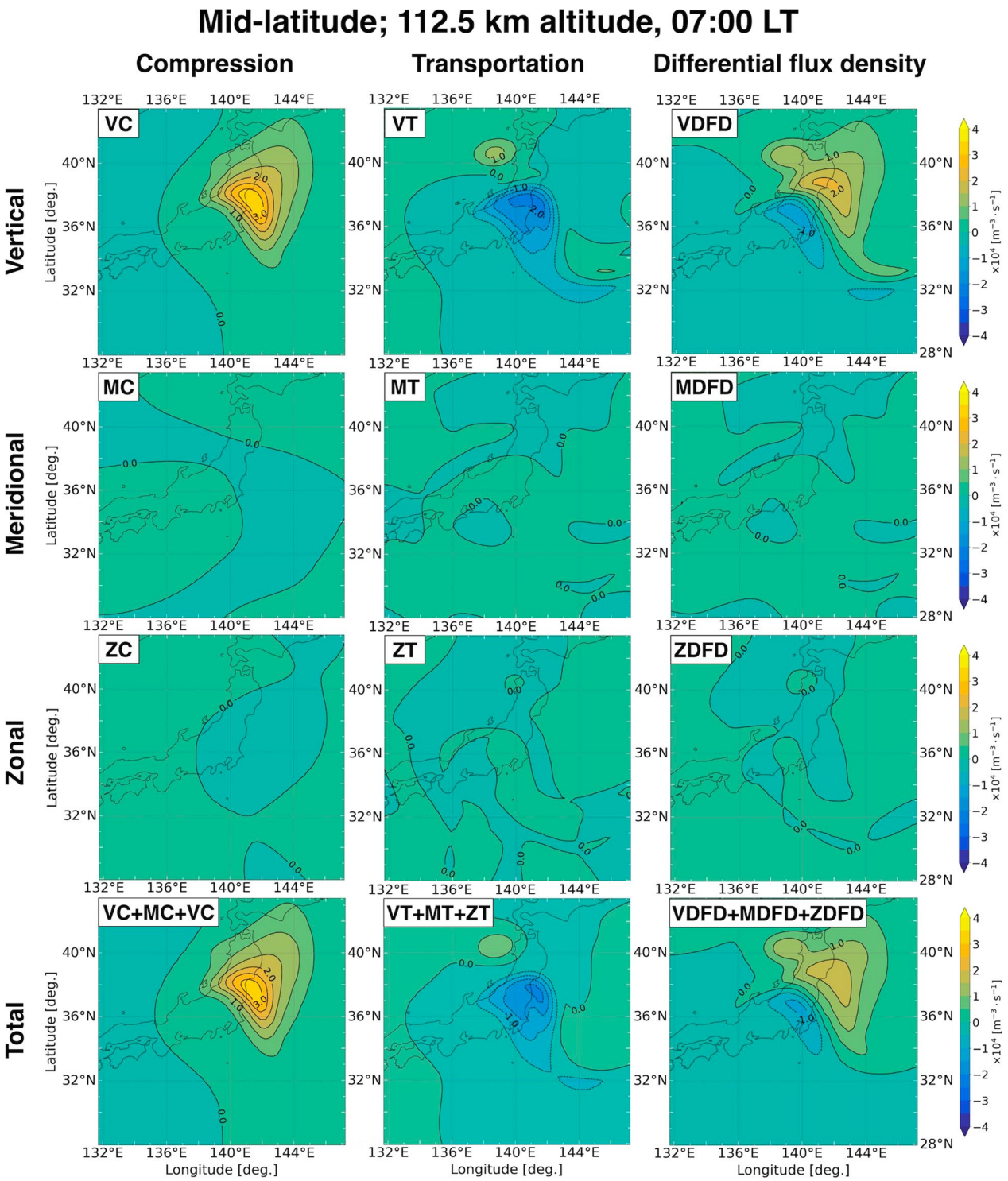

Fig. 3 Horizontal distributions at 112.5 km altitude and 7 LT of the compression, transportation, and differential flux density (first, second, and third columns). The first, second, and third rows show density variations due to vertical dynamics (VC, VT, and VDFD), meridional dynamics (MC, MT, and MDFD), and zonal dynamics (ZC, ZT, and ZDFD), respectively. The fourth row shows the total variables displayed in the first, second, and third rows. The color range is between -4.0×10^4 and 4.0×10^4 $m^{-3}\,s^{-1}$

above ~110 km, the structural variations in the Es layers are ascribed to those of the vertical zonal-wind shears. Hence, hereafter, we focus on horizontal Es movements below ~110 km driven by diurnal and semi-diurnal tides.

We note that ions can be transported by horizontal winds above ~110 km; however, for Es layer dynamics, horizontal transport is negligible compared to vertical transport and compression above ~110 km, as shown in Fig. 3. This is because vertical ion convergence time is small above ~110 km. In other words, the ion gyrofrequency is not small in relative to ion–neutral collision frequency above ~110 km. Above ~110 km, Es layers are formed generally at the location where vertical ion convergence is strong, and not move with neutrals.

Figure 4 shows the same results as Fig. 2 but at 103 km and 17 LT. Figure 4a displays the horizontal distribution of the stagnating Es layer (SEsL) at ~103 km in Fig. 1a, whose altitude and local time are denoted by the magenta cross at 17 LT. In Fig. 4a, the Es layer extends from 28°N and 147°E to the northwest. The Es layer is present near, but not constrained at the geomagnetic zonal-wind shear nodes because it ascends by the Lorentz force due to the geomagnetic eastward winds after 16 LT, as shown in Fig. 1a. The Es layer is located in the weak zonal wind regions (within ±12.5 m/s), Fig. 4b. It spreads over the northward and southward wind regions, Fig. 4c. We note that the horizontal velocity of the Es layer was generally equivalent to the horizontal wind velocity below ~ 110 km.

Figure 5 shows the same results as Fig. 3, but at 103 km and 17 LT. The color range is between -1.5×10^5 and 1.5×10^5 m^{-3} s^{-1}. The color range is greater than that shown in Fig. 3 because the Es layer becomes denser as it descends. In the first column, VC is on the order of 10^5 m^{-3} s^{-1}, and MC and ZC are on the order of 10^4 m^{-3} s^{-1}. VC is greater than MC and ZC. It should be noted that the ratio of VC to MC and ZC decreases in Fig. 5, compared to that in Fig. 3. This is because, below ~110 km, the ion gyrofrequency becomes much smaller than the ion–neutral collision frequency (Haldoupis 2011), and the vertical ion movements driven by the Lorentz force are inhibited by frequent ion–neutral collisions, compared to those at higher altitudes. The total VC, MC, and ZC are generally equivalent to VC. In the second column, MT is equivalent to VT on the order of 10^5 m^{-3} s^{-1}. As asserted above, this is because of the frequent ion–neutral collisions. However, ZT, whose order is 10^4 m^{-3} s^{-1}, is smaller than MT and VT because the Es layer exists near the zonal wind-shear nodes as shown in Fig. 4a and 4b. Thus, in horizontal movements, the Es layer is prone to move in the meridional direction rather than in the zonal direction. The direction of the horizontal Es movement can be estimated from the MT. A negative MT appears at around 32°N and 146°E. A positive MT appears at around 31°N and 146°E. The positional relationship between the negative and positive MT regions indicates southward Es movements, which correspond to the meridional wind direction. In the third column, VDFD and MDFD are greater than ZDFD, and their total is approximately the summation of VDFD and MDFD. Compared to the Es layer above 110 km, the Es layer below 110 km is affected more significantly by the horizontal ion dynamics.

In Fig. 5, we showed that the Es layers can be transported by the meridional winds below ~110 km. In addition, they can be transported by zonal winds when the

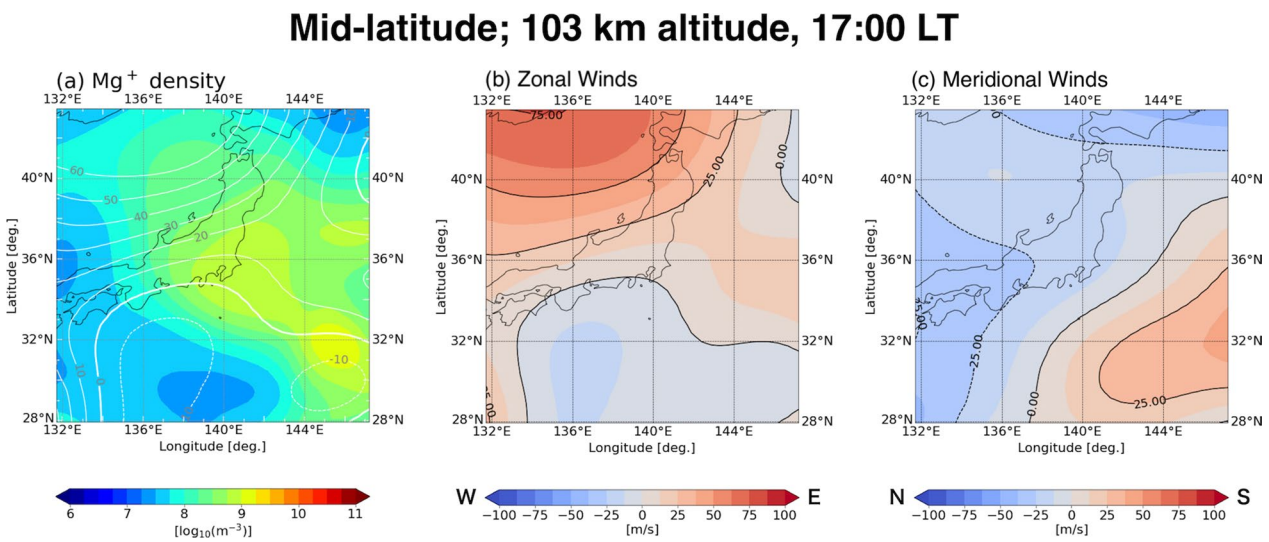

Fig. 4 Horizontal distributions as in Fig. 2, but at 103 km and 17 LT

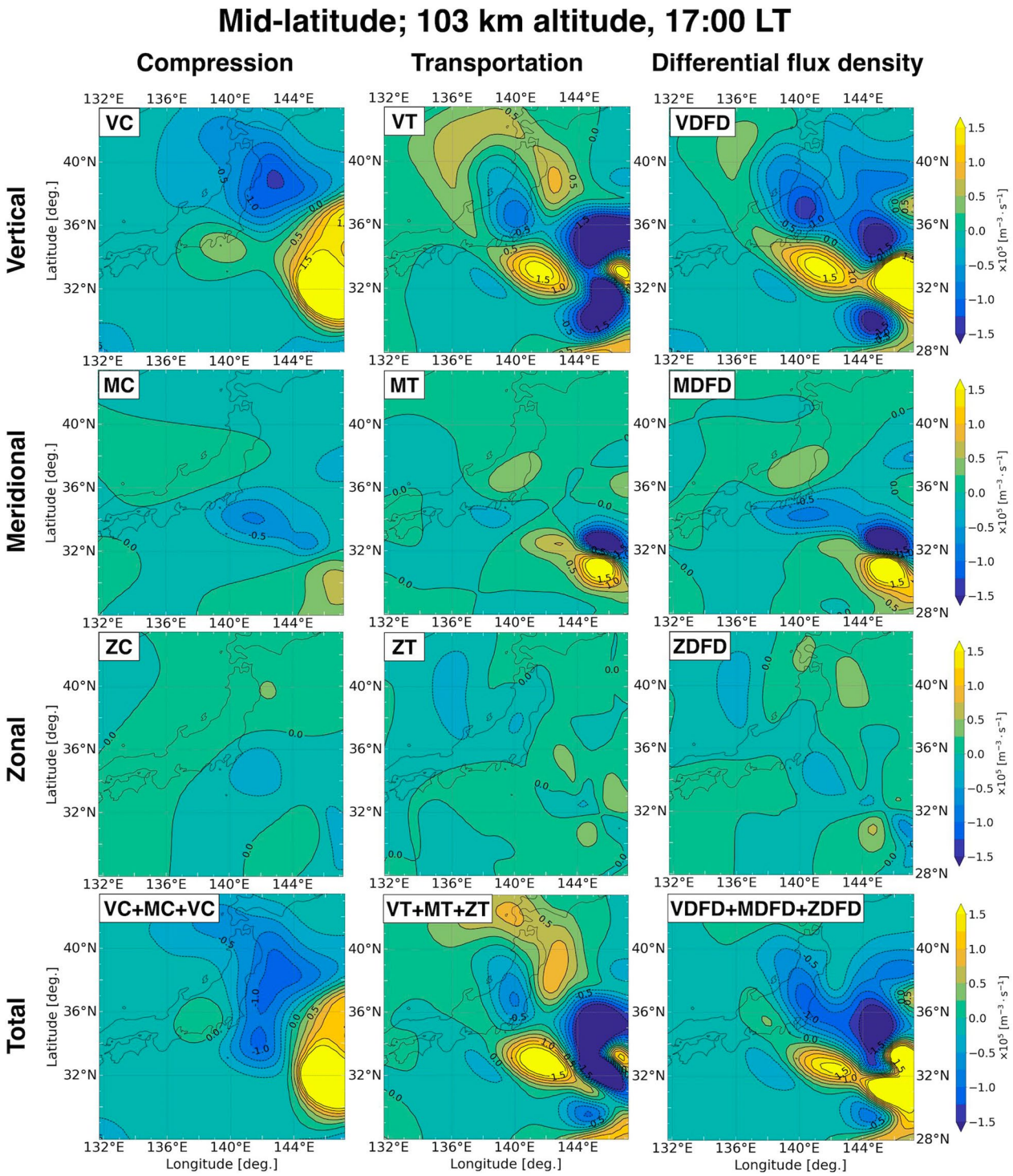

Fig. 5 Horizontal distributions as in Fig. 3, but at 103 km and 17 LT. The color range is between -1.5×10^4 and 1.5×10^4 m^{-3} s^{-1}

layers deviate from the zonal-wind shear nodes. Below ~ 110 km, the Es layers lag behind the geomagnetic zonal-wind shear nodes, which generally correspond to zonal-wind shear nodes. Consequently, they are left in the westward wind regions. The upper three panels in Fig. 6 show the horizontal distributions at 107 km and 3 LT of (a) Mg^+ ion, (b) zonal, and (c) meridional winds to show the zonal movements of the Es layers. The altitude and

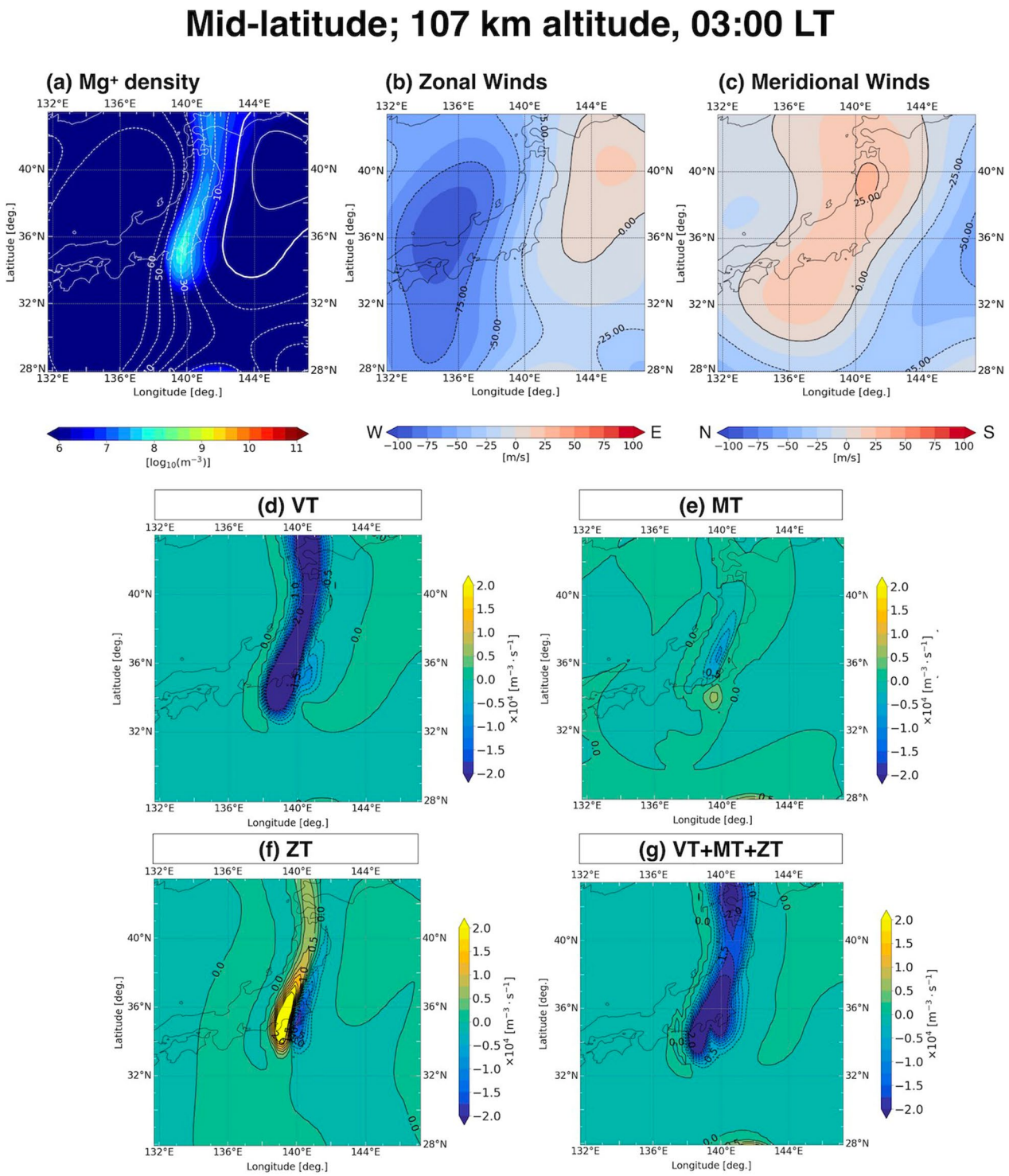

Fig. 6 The upper three panels show the horizontal distributions at 107 km and 3 LT of **a** Mg^+ density, **b** zonal, and **c** meridional winds. The lower four panels show the **d** vertical, **e** meridional, **f** zonal, and **g** total transportation of the Es layer in Fig. 6a. The color range is between -2.0×10^4 and 2.0×10^4 m^{-3} s^{-1}

local time are denoted by the magenta cross at 3 LT in Fig. 1a. As shown in Fig. 1a, the Es layer, whose horizontal distribution is displayed in Fig. 6a, deviates from the geomagnetic zonal-wind shear nodes. From Fig. 6b and c, the Es layer is located in the westward and southward wind regions. The meridional winds are smaller than ∼ 25 m/s southward, and zonal winds are nearly 50 m/s westward. The lower four panels in Fig. 6 show the (d) vertical, (e) meridional, (f) zonal, and (g) total transportation of the Es layer in Fig. 6a. The order of VT and ZT is 10^4 m^{-3} s^{-1}, and MT is 10^3 m^{-3} s^{-1}. Clearly, ZT is equivalent to VT, and total transportation is generally the summation of ZT and VT. This indicates that the Es layer moves westward as it lags behind the geomagnetic zonal-wind shear nodes.

As a brief summary, below ∼110 km, MT and/or ZT become equivalent to VC and VT. Thus, the Es layers below ∼110 km are transported horizontally by local winds. The Es layer movement direction is determined by the wind direction. The DEsLs are embedded in the southward wind regions, and move southward, as shown in Fig. 5. Lagging behind the geomagnetic zonal-wind shear nodes, the DEsLs become embedded in the westward wind regions and to move westward, as shown in Fig. 6. The SEsLs at ∼100 km, which deviate from the geomagnetic zonal-wind shear nodes, are horizontally transported by semi-diurnal tides there. Considering the phase variations in the semi-diurnal tides, Fig. 1b, the SEsLs tend to move westward at 9–15 and 21–3 LT, and eastward at 3–9 and 15–21 LT. From Fig. 1c, the SEsLs tend to move southward during pre-noon and pre-midnight and northward during post-noon and post-midnight.

Horizontal Es movements driven by diurnal tides

Figure 7 shows the horizontal distributions of (a) Mg^+ density, (b) zonal winds (eastward positive), and (c) meridional winds (southward positive) at low-latitudes around Arecibo at 103 km and 6 LT. The Es structure corresponds to the lower Es layer in Fig. 1d, whose altitude and local time are denoted by the magenta cross at 6 LT. The contours in Fig. 7a represent the geomagnetic zonal wind velocity. The Es layer shows a two-banded structure; the southern one elongates between 59° and 68°W in the east–west direction, and the northern one elongates between 59° and 68°W in the northwest–southeast direction. The two-banded structure exists near, but is not constrained at, the geomagnetic zonal-wind shear nodes, where the geomagnetic zonal wind velocity is zero. The two-banded Es structure is embedded in the westward wind regions, as shown in Fig. 7a and b. However, the westward wind is weak (within ±12.5 m/s). The layer is embedded in the southward wind regions, Fig. 7c. The southward winds exceed 50 m/s.

Figure 8 shows the same results as Fig. 3, but at 103 km and 6 LT at low-latitudes around Arecibo. Its color range is between -2.0×10^7 and 2.0×10^7 m^{-3} s^{-1}. In the first column, VC is on the order of 10^7 m^{-3} s^{-1}, and ZC and MC is on the order of 10^6 m^{-3} s^{-1}. Thus, VC driven by diurnal tides is greater than MC and ZC. The total compression in the fourth row is equivalent to VC. In the second column, MT and VT are on the order of 10^7

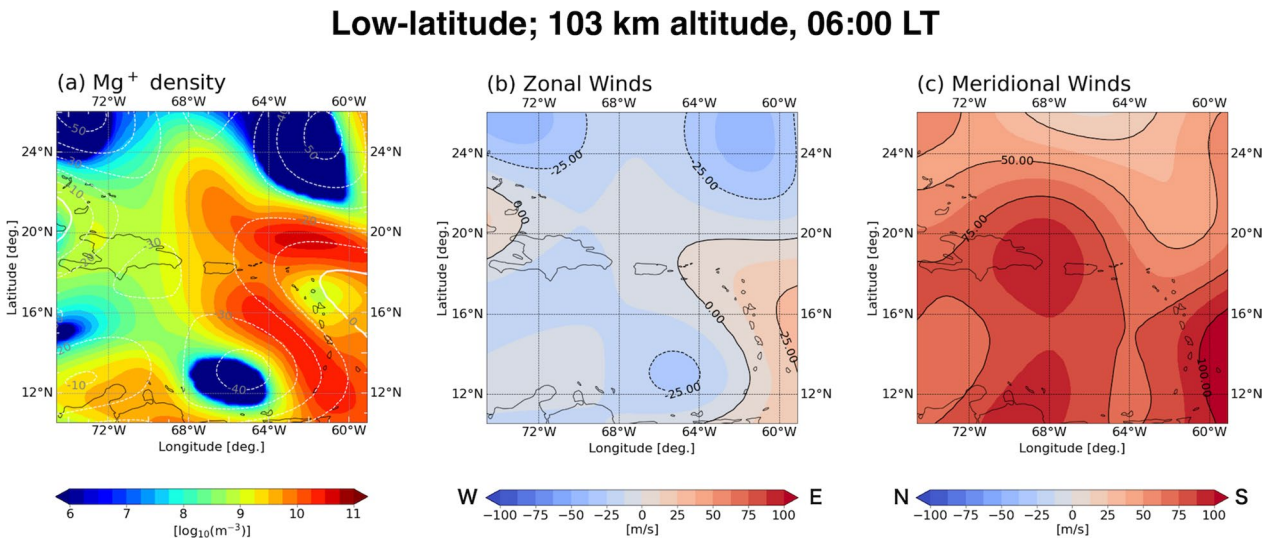

Fig. 7 Horizontal distributions of **a** Mg^+ density, **b** zonal winds (eastward positive), and **c** meridional winds (southward positive) at low-latitudes around Arecibo at 103 km and 6 LT. The Es structures correspond to the lower Es layer in Fig. 1d. The contours in Fig. 7a represent the geomagnetic zonal wind velocity

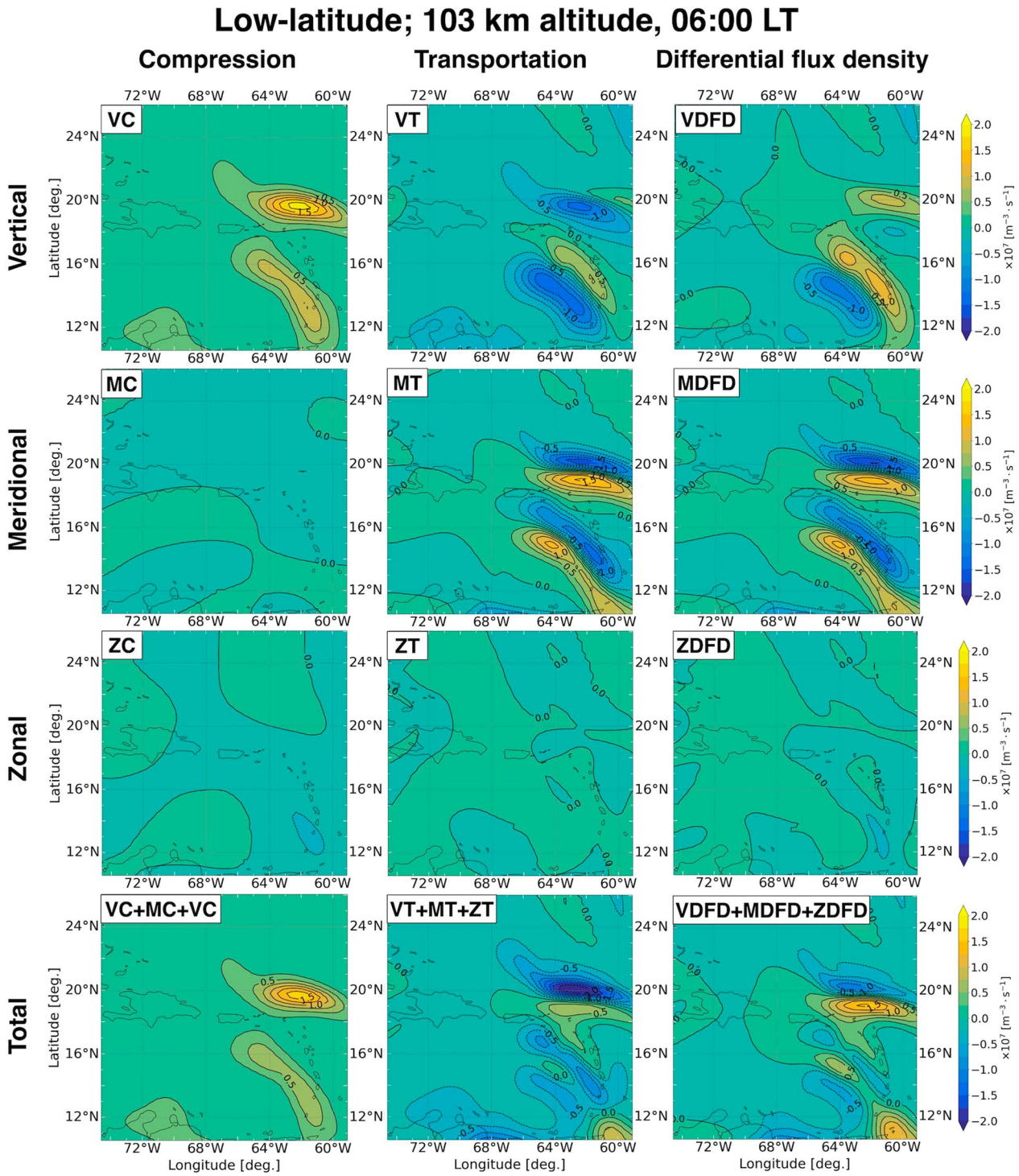

Fig. 8 Horizontal distributions as in Fig. 3, but at 103 km and 6 LT at low-latitudes around Arecibo. The color range is between -2.0×10^7 and 2.0×10^7 m^{-3} s^{-1}

m^{-3} s^{-1}, and ZT is on the order of 10^6 m^{-3} s^{-1}. MT is equivalent to VT, which is the same as in the mid-latitude case. ZT is smaller than MT because the lower Es layer is located generally in the regions where the zonal wind velocity is zero, as shown in Fig. 7a and b. In the third column, VDFD and MDFD are greater than ZDFD. The

total differential flux density in the fourth row is nearly equal to the summation of VDFD and MDFD. The lower Es layer in Fig. 1d is generated by the vertical compression due to the geomagnetic zonal-wind shear driven by diurnal tides. However, under strong vertical wind-shears driven by diurnal tides, the lower Es layer can be modified by horizontal transport due to the horizontal winds; therefore, its behavior cannot be explained only by vertical ion dynamics, as in the mid-latitude case.

Discussion

3D ionospheric simulations at mid- and low-latitudes were performed to reveal the horizontal movements of the Es layers driven by diurnal and semi-diurnal tides. We found that above ~110 km, the spatial and temporal variations in the Es layers are controlled mainly by VC and VT, as shown in Fig. 2. VC is equivalent to VT, whose order is 10^4 m^{-3} s^{-1}. The horizontal Es movements above ~110 km are not influenced by horizontal compression and transport, on the order of 10^2 m^{-3} s^{-1} (MC, ZC, and ZT) and 10^3 m^{-3} s^{-1} (MT). Below ~110 km, horizontal transport is equivalent to VT and VC, as shown in Figs. 5, 6 and 8. In Figs. 5 and 8, the order of the VC, VT and MT is 10^5 and 10^7 m^{-3} s^{-1}, and that of MC, ZC, and ZT is 10^4 and 10^6 m^{-3} s^{-1}, respectively. Comparing MT and ZT for the DEsLs, MT is generally larger than ZT because the Es layers are formed near the zonal-wind shear nodes. However, as shown in Fig. 6, the more the Es layers deviate from the geomagnetic zonal-wind shear nodes, the more frequently they move westward.

From Figs. 3, 5, 6, and 8, it was revealed that, below ~ 110 km, the Es layers are transported by the local winds. To summarize the horizontal Es movements, a schematic

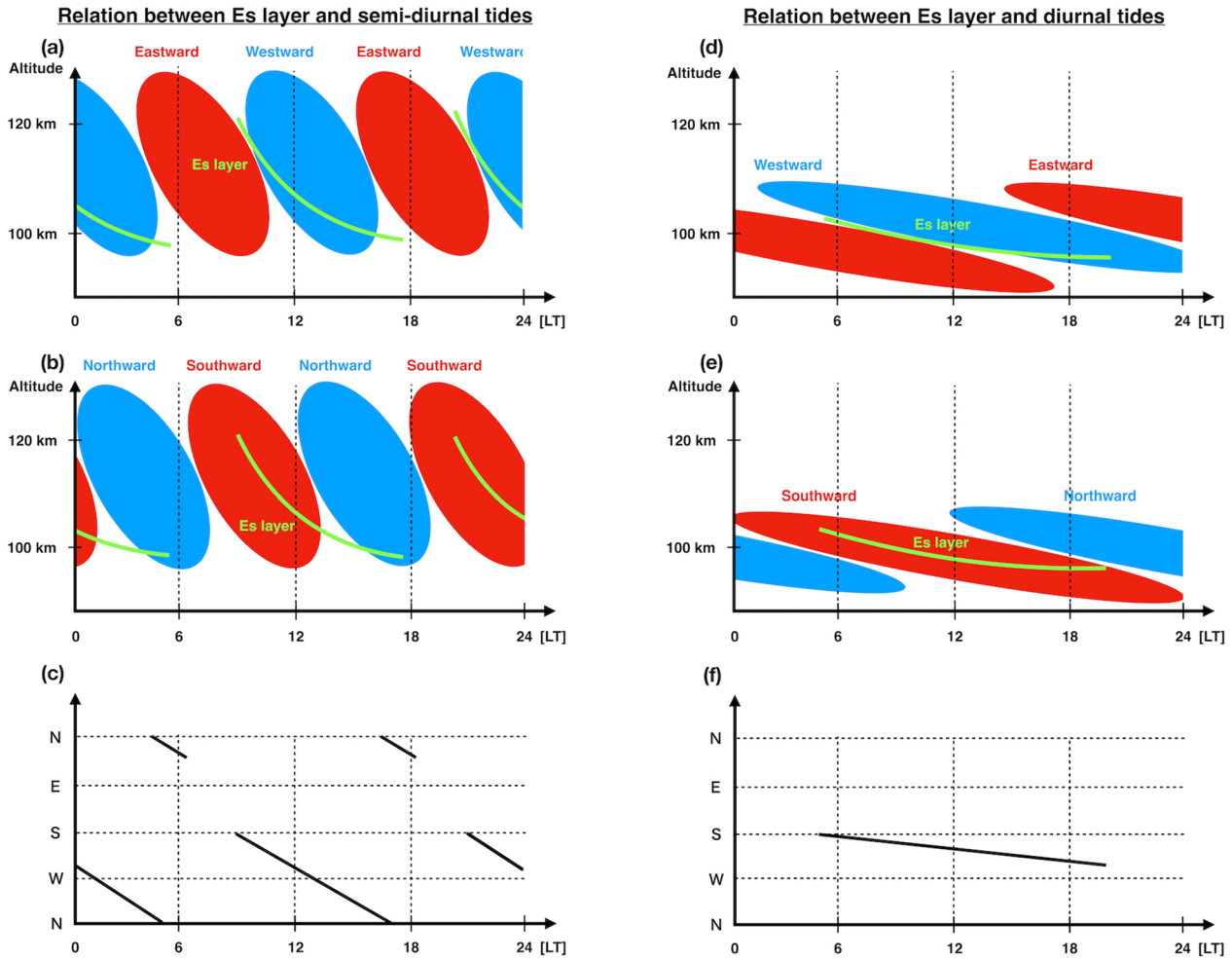

Fig. 9 Schematic diagram of relationships between Es layers and **a**, **b** semi-diurnal tides and **d**, **e** diurnal tides. The top plots **a** and **d** display the Es layers and the zonal tide component. The middle plots display the Es layers and the meridional tide component. The vertical axis represents altitude and horizontal axis represents local time. The black lines in the bottom panels **c** and **f** indicate the temporal variations in the movement directions (N, W, S, and E) of the Es layers due to the tides

diagram of relationships between Es layers and (a-b) semi-diurnal tides and (d-e) diurnal tides is shown in Fig. 9. The top plots illustrate the relationship between the Es layers and zonal winds of the tides, and the middle plots illustrate that of the Es layers and meridional winds of the tides. The vertical axis represents altitudes, and the horizontal axis represents local time. The black lines in the bottom panels, 9c and 9f, indicate the temporal variations in the movement directions (N, W, S, and E) of the Es layers due to tides. In other words, the black lines indicate the wind directions at the heights of the Es layers in the top and middle rows of Fig. 9.

In Fig. 9a, the Es layers are formed near the zonal-wind shear nodes of the semi-diurnal tides above ~110 km in the pre-noon and pre-midnight sectors, as the Es layer in Fig. 2. The Es layers descend and lag behind the nodes, and become embedded in the westward wind regions at 9–15 LT and 21–3 LT, as the Es layer in Fig. 6. Subsequently, the Es layers stagnate at approximately 100 km after noon and midnight. Thus, the Es layer can move eastward roughly after 6 LT and 18 LT, as that in Fig. 3. In Fig. 9b, given the rotational tidal phase variations, the DEsLs exist in the southward wind regions primarily during the pre-noon and pre-midnight periods. Therefore, the Es layers formed by semi-diurnal tides tend to move southward while they descend. When the Es layers stagnate at ~100 km, they move northward during the post-noon and post-midnight periods. The Es movements caused by the semi-diurnal tides are summarized by black lines in Fig. 9c.

SEsLs around 100 km are expected to be blown by the zonal winds of semi-diurnal tides. They move westward rather than eastward. As shown in Fig. 9, the SEsLs penetrate from the westward/southward wind regions into the westward/northward wind regions after ~12 and 24 LT. In the westward/northward wind regions, the metal ions diverge vertically, and Es layers decrease in density. Most Es layers disappear in this region. Few Es layers can further penetrate the eastward/northward wind region, roughly after 6 and 18 LT. The sparse metal ions ascend to above 110 km because of the upward Lorentz force driven by the eastward winds. In the eastward/southward wind region, metal ions converge vertically at approximately 120 km. As shown in the present simulation, Fig. 1a, the SEsL at ~103 km diffuses after ~ 17 LT in the eastward/northward wind regions. The diffused metal ions gather and form a nighttime Es layer in the southward/westward wind regions.

In Fig. 9d, the Es layer forms near the zonal-wind shear nodes of the diurnal tides around dawn. The Es layer descends and lags behind the nodes, and exists in the westward wind regions at a local time of 6–18 h. In Fig. 9e, as in the semi-diurnal tide case, the Es layer exists in the southward wind regions at a local time of 6–18 h. Thus, the Es layer formed by diurnal tides tends to move southward, as the Es layer in Fig. 7. The Es layer hardly moves eastward or northward. This is because, even if it stagnates below 100 km, the density of the Es layer decreases rapidly owing to the three-body reactions of metal ions before being blown by the eastward or northward winds. These Es movements are summarized by a black line in Fig. 9f.

To further confirm the horizontal Es movement shown in Fig. 9, we show the 3D trajectory of the metal ions comprising the DEsL and SEsL from 8 to 17 LT on June 3, 2015 at mid-latitudes. The trajectories of the metal ions were calculated using the simulated 3D ion velocity. The trajectory started at 8 LT when the DEsL began to be formed at an altitude of 110 km, 38.45°N, and 138.2°E. It ended at 17 LT, 97.5 km altitude, 38.45°N, and 133.7°E because the SEsL diffused and became non-visible after 17 LT, as with the SEsL in Fig. 1a. The upper panel of Fig. 11 shows the 3D trajectory of the metal ions within the DEsL and SEsL. The lower left three panels display the altitude, latitude, and longitude variations in the metal ion trajectory. The lower right panel displays the zonal/meridional ion velocity along the trajectory (eastward/southward positive).

At the beginning of the trajectory, at 8 LT, the metal ions converge in an altitude of 110 km (38.45°N and 138.2°E). The converging metal ions form the DEsL. The DEsL descends to ~100 km at 12 LT (35.7°N and 136.9° E). After ~12 LT, the DEsL becomes the SEsL, which persists at ~100 km, as shown in the trajectory altitude panel. The SEsL moves horizontally as shown in the trajectory latitude and longitude panel. At the end of the trajectory, at 17 LT, the SEsL is present at 97.5 km (38.45°N and 133.7°E). From the lower right panel, the DEsL, which corresponds to the trajectory between 8 LT and 12 LT, moves southward and westward. As time passed, the westward velocity of the DEsL gradually increases, which indicates that the DEsL lags behind the zonal-wind shear nodes. The meridional movement of the SEsL, which corresponds to the trajectory after 12 LT, turns from southward to northward after 13 LT. The SEsL always moves westward. We note that the horizontal ion velocity approximately equals the horizontal wind velocity. These horizontal Es movements are consistent with the horizontal Es movements in the lower left panel of Fig. 9. The horizontal movements of the overall Es layers can be described schematically as Fig. 9.

We emphasize that horizontal Es movements are affected by both semi-diurnal and diurnal tides. Thus, we must consider the relationship between the Es layers and semi-diurnal/diurnal tides in Fig. 9 at the same time. Moreover, neutral winds in the mesosphere and lower

thermosphere (MLT) region result from the superposition of both semi-diurnal/diurnal tides and other small-scale gravity waves (Liu et al. 2014; Yiğit and Medvedev 2017). Semi-diurnal and diurnal tides exhibit day-to-day variability (Miyoshi and Fujiwara 2003; Pedatella et al. 2012). To investigate the horizontal Es movements, the above-mentioned variations in the neutral winds in the MLT region, in addition to the relation presented in Fig. 9, must be considered.

The present simulations revealed that the Es movements above ~110 km are not attributed to horizontal wind transport, but to vertical structural Es variations. This result does not dispute previous observations of horizontal Es movements. This is because radio waves and total electron content (TEC) observations can detect denser Es layers more frequently. Sparse Es layers may be difficult to observe using such techniques. It is known that most Es layers become denser as they descend and exhibit their maximal density below 110 km (Haldoupis et al. 2020). For this reason, most previous studies aimed to observe horizontal Es movements below ~110 km (e.g., Tanaka 1979; Maeda and Heki 2015; Sun et al. 2021).

Previous observations have reported that Es layers have a westward moving tendency (Koizumi 1969; Beynon et al. 1972; Tanaka 1979; Sun et al. 2021). We found that the DEsLs move westward rather than eastward because they lag behind the geomagnetic zonal-wind shear nodes that form the Es layers. However, we should point out the differences between geomagnetic and geographic zonal winds owing to the declination of geomagnetic fields. This is because metal ions gather in the geomagnetic zonal-wind shear nodes to form the Es layers, but not the geographic zonal-wind shear nodes. It should be noted that, in this paragraph, we explicitly use "geographic" to avoid any confusion. The geographic zonal winds (u_n) and geographic meridional winds (v_n) driven by atmospheric tides are described by the following equations (Mathews and Bekeny 1979; Haldoupis et al. 2006):

$$u_n = -V_0 \sin\left(\frac{2\pi}{\lambda_z}z + \phi_t\right), \tag{14}$$

$$v_n = V_0 \cos\left(\frac{2\pi}{\lambda_z}z + \phi_t\right), \tag{15}$$

where V_0 is the maximum amplitude, λ_z is the vertical wavelength, and ϕ_t is the time-dependent phase of the tides, and z is the altitudes. Thus, using Eqs. 13–15, the geomagnetic zonal winds driven by the tides are calculated as:

$$\begin{aligned} u_m &= -V_0 \sin\left(\frac{2\pi}{\lambda_z}z + \phi_t\right)\cos D + V_0 \cos\left(\frac{2\pi}{\lambda_z}z + \phi_t\right)\sin D \\ &= -V_0 \sin\left(\frac{2\pi}{\lambda_z}z - D + \phi_t\right). \end{aligned} \tag{16}$$

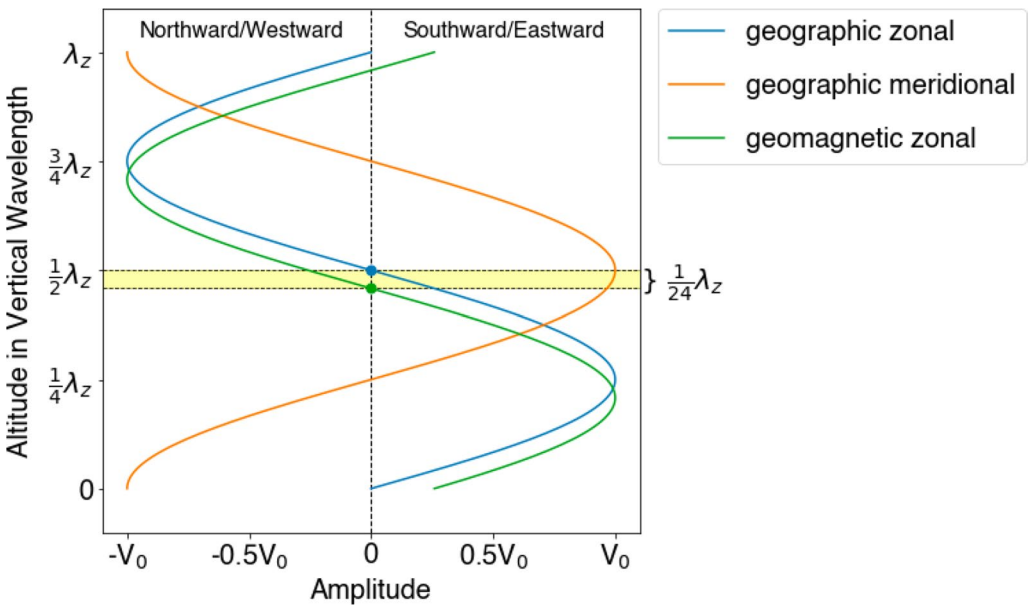

Fig. 10 Relation of the geomagnetic/geographic zonal winds and geographic meridional winds driven by the atmospheric tides calculated by Eqs. 14, 15, 16. The vertical axis represents the altitude in the vertical wavelength, and the horizontal axis represents tidal amplitudes. The geomagnetic and geographic zonal-wind shear node is highlighted by the green and blue dots, respectively. The deviation of the two nodes is highlighted in yellow

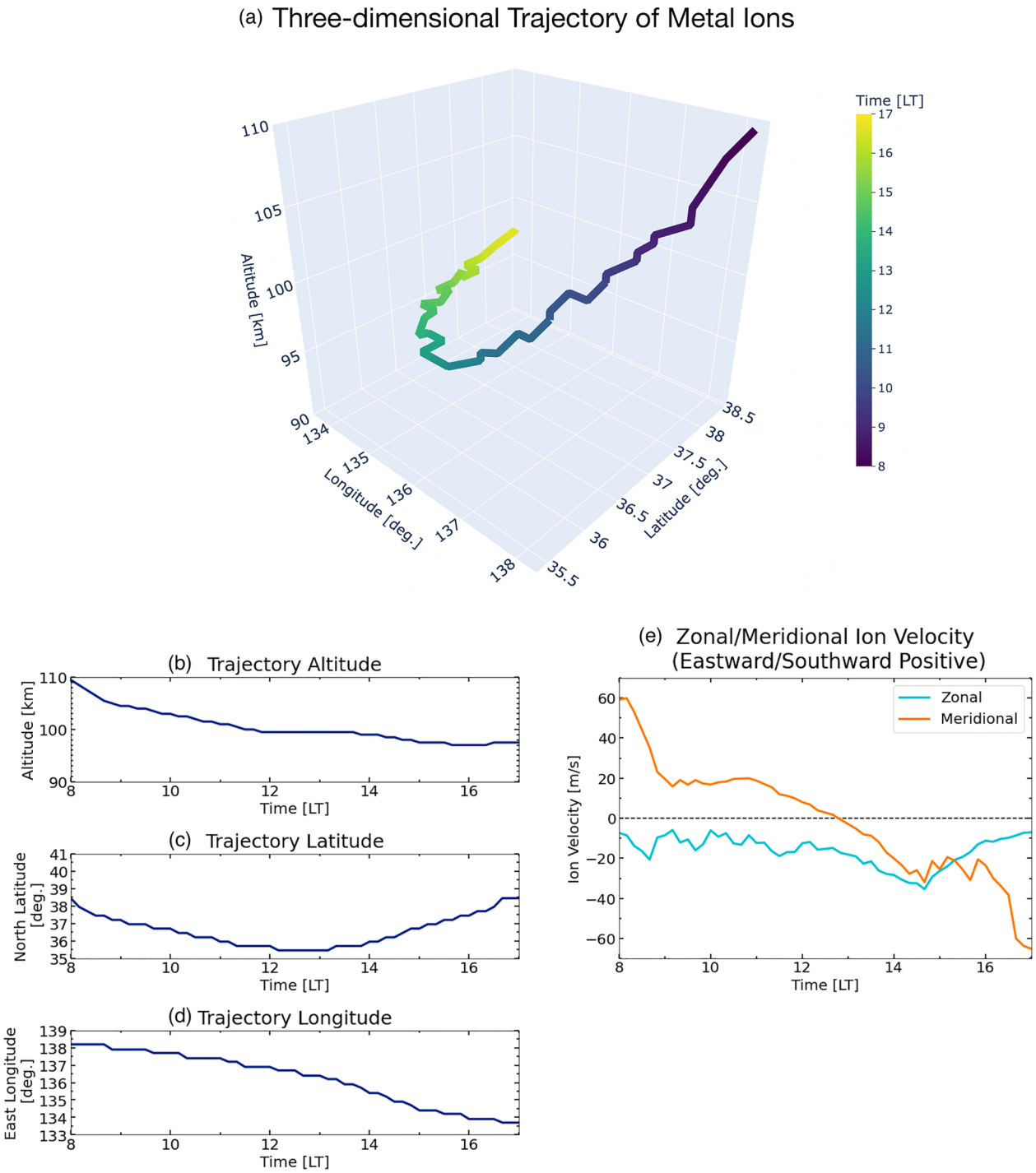

Fig. 11 **a** 3D trajectory of the metal ions. **b** Altitude trajectory variation. **c** Latitude and **d** longitude trajectory variation. **e** Zonal/meridional ion velocity along the trajectory (eastward/southward positive)

The positive directions of the geomagnetic/geographic zonal winds and geographic meridional winds are geomagnetic/geographic eastward and southward, respectively. Figure 10 depicts the relationship among u_n, v_n, and u_m at an arbitrary time. We assumed that D was -15 degrees, which generally corresponds to the largest declination around the eastern America at geomagnetic

mid-latitudes (Thébault et al. 2015). The vertical axis represents the vertical tidal wavelength altitude. The horizontal axis represents the tidal amplitude. The geomagnetic and geographic zonal-wind shear nodes are indicated by the green and blue dots, respectively. The deviation of the two nodes is highlighted in yellow. The deviation between the two nodes was calculated as $\frac{\lambda_z}{24}$. Estimated from Fig. 1b, c and e, f, the vertical wavelength of the semi-diurnal and diurnal tides is approximately 60 km and 25 km, respectively. As shown in Fig. 10, the Es layers can move geographically eastward, at the geomagnetic zonal-wind shear nodes. However, DEsLs can have a westward movement tendency because the Es layers descend and lag behind the geomagnetic zonal-shear nodes (Haldoupis 2011, 2012; Andoh et al. 2020, 2021). This indicates that the Es layers move into the geographic westward wind regions over time. Therefore, lagging behind the nodes, the Es layers move geographically westward more frequently than eastward. It should be noted that around the great negative declination region, such as in the South Atlantic anomaly, the Es layers may move more frequently in the eastward direction.

Beynon et al. (1972) and Tanaka (1979) observed the eastward Es movements in addition to the westward tendency of the Es movements. This is not compatible with observations in which the Es layers move westward rather than eastward (Koizumi 1969; Sun et al. 2021). The discrepancy of the zonal Es movements among the previous observations can be explained by the local time and Es layer altitudes, as shown in Fig. 9. Given the relationship shown in the left column of Fig. 9, intense SEsLs may be sustained in the eastward wind regions after 6 and 18 LT. This time-dependent eastward Es movement coincides generally with the movement direction variations presented in Beynon et al. (1972) and Tanaka (1979). Beynon et al. (1972) reported that the Es layers moved eastward generally after 7 and 16 LT except in November, when they moved eastward after 13 LT. Tanaka (1979) observed eastward Es movements after 6 and 18 LT, in addition to around 12 LT. Some inconsistencies between our simulations and the previous observations may be caused by the day-to-day variations in the tides and/or atmospheric gravity waves (Miyoshi and Fujiwara 2003; Pedatella et al. 2012; Liu et al. 2014; Yiğit and Medvedev 2017).

The discrepancy between the observed meridional Es movements can also be described by the local time and Es layer altitudes. Recent TEC observations showed a controversial result that all the Es layers move southward around China (Sun et al. 2021) or the Es layers are blown by semi-diurnal tides around Japan (Maeda and Heki 2015). Maeda and Heki (2015) proposed that Es layers move mainly northward in 10–14 LT and mainly southward in 17–19 LT. Their results seem not to correspond to our summarized results in Fig. 9. However, we emphasize that the Es layers in Fig. 9 are just an example. The descending velocity and stagnation altitudes of Es layers can be different in reality. Based on the meridional phase variations of semi-diurnal tides in Fig. 9, SEsLs between 100 and 110 km can move northward in 12–18 LT and southward in 18–24 LT. Further, considering day-to-day variations of semi-diurnal tides such as presented in Fig. 1c, our results can explain horizontal Es movements presented in Maeda and Heki (2015). Sun et al. (2021) clearly observed DEsLs, but not SEsLs, as shown in their Fig. 7. The observed Es layers move southward and not northward, which is consistent with our simulated descending layers at mid- and low-latitudes. Overall, to discuss the horizontal Es movements, we must consider the Es layer altitude and the local time, as in Sun et al (2021).

It should be noted that Maeda and Heki (2014, 2015) investigated smaller-scale Es structures than Sun et al (2021). In our simulations, the Es structures whose scale is smaller than a hundred kilometers were not reproduced well due to the coarse neutral wind resolution. Es layers can be affected by atmospheric gravity waves (e.g., Chimonas 1971; Obenberger et al 2021). Thus, the horizontal Es movements presented in Maeda and Heki (2014, 2015) might result from phase propagations of atmospheric gravity waves, as with the traveling ionospheric disturbances (Miyoshi et al 2018). We need to further investigate horizontal Es movements driven by other factors than atmospheric tides to reveal comprehensive mechanisms of horizontal Es movements.

At low-latitudes, Es layers formed by diurnal tides are more frequently observed than those formed by semi-diurnal tides (Christakis et al 2009) because diurnal tides are stronger and semi-diurnal tides are weaker at low-latitudes than at mid-latitudes (Hagan and Forbes 2002; Oberheide et al 2015; Solomon and Roble 2015). This indicates that DEsL can be observed more frequently at low-latitudes than at mid-latitudes. We suggest that the low-latitude Es layers may move southward more frequently than the mid-latitude Es layers do. The horizontal Es movements can have latitudinal dependence.

We note that horizontal Es movements can be affected not only by diurnal and semi-diurnal tides but also by higher-order tides such as terdiurnal and quarter-diurnal tides. Previous studies indicated that EsL dynamics can be affected by terdiurnal and quarter-diurnal tides in

some seasons (e.g., Haldoupis et al 2006; Haldoupis and Pancheva 2006; Jacobi et al 2019; Oikonomou et al 2022). Terdiurnal and quarter-diurnal tides may influence seasonal variations of horizontal Es movements. To confirm this, more simulations and observations of horizontal Es movements are necessary for all seasons. This is future work.

Conclusion and summary

We attempted to reveal horizontal Es movements driven by atmospheric diurnal/semi-diurnal tides using a 3D ionospheric model. There have been no comprehensive studies to explain the different results of horizontal Es movements asserted from a variety of observations. Moreover, horizontal Es movements have been deduced from 1D or 2D observations. To assess the horizontal Es movements from a 3D perspective, in this study, we performed 3D Es simulations at mid- and low-latitudes.

Horizontal Es movements are driven by two different mechanisms depending on altitudes. We found that the Es layers are constrained at the zonal-wind shear nodes above ~110 km, and horizontal Es movements above ~ 110 km result from spatio-temporal variations of vertical ion convergence regions. In contrast, Es layers are transported horizontally by horizontal winds below ~110 km. Below ~110 km, the Es layers that descend with the downward diurnal/semi-diurnal tide phases move southward and westward. The DEsLs tend to move southward rather than westward because they occur near the zonal-wind shear nodes, where the zonal wind velocity is zero. As the DEsLs lag behind the zonal-wind shear nodes, the layers become embedded in the westward wind regions, and move westward. When the Es layers stagnate at ~ 100 km, they can move in the meridional and zonal directions with diurnal/semi-diurnal tidal phase variations. In general, the DEsLs and SEsLs do not move eastward. This is because the Es layers diffuse vertically in the eastward/northward wind region and are in the early stage of forming in the eastward/southward wind region. The horizontal Es movement mechanism revealed by this study agrees with and provides a general explanation for previous observations.

Abbreviations

DEsL	Descending Es layer
Es	Sporadic E
GAIA	Ground-to-topside model of Atmosphere and Ionosphere for Aeronomy
IPPs	Ionospheric pierce points
MC	Meridional compression
MDFD	Meridional differential flux density
MLT	Mesosphere and lower thermosphere
MT	Meridional transportation
SEsL	Stagnating Es layer
TEC	Total electron content
VC	Vertical compression
VDFD	Vertical differential flux density
VT	Vertical transportation
ZC	Zonal compression
ZDFD	Zonal differential flux density
ZT	Zonal transportation
3D	Three-dimensional

Acknowledgements

This work is supported by "Nagoya University High Performance Computing Research Project for Joint Computational Science" in Japan and Grant-in-Aid for JSPS Fellows (JP21J13173). We thank the GAIA project, which is carried out by the National Institute of Information and Communications Technology, Kyushu University, and Seikei University, for providing the neutral wind data.

Author contributions

SA developed the ionospheric numerical model for metal ion layers and conducted the simulations, and wrote the paper. AS supervised this study and contributed to revise the paper. HS prepared datasets used in this study and contributed to revise the paper. All authors read and approved the final manuscript.

Funding

Funding was provided by Grant-in-Aid for JSPS Fellows (G).

Availability of data and materials

The Ap and F10.7 indices for the simulated days were provided by the Data Analysis Center for Geomagnetism and Space Magnetism, Kyoto University (http://wdc.kugi.kyoto-u.ac.jp/kp/index.html) and NOAA/NCEI (https://www.ngdc.noaa.gov/stp/space-weather/solar-data/solar-features/solar-radio/noontime-flux/penticton/penticton_observed/tables/), respectively. All the data used in this study are available at https://doi.org/10.14989/266477 and https://doi.org/10.57723/273978.

Declarations

Competing interests

The authors declare that they have no competing interests.

Author details

[1]Graduate School of Science, Kyoto University, Kyoto, Japan. [2]National Institute of Information and Communications Technology, Tokyo, Japan. [3]International Research Center for Space and Planetary Environmental Science, Kyushu University, Fukuoka, Japan.

Received: 5 December 2022 Accepted: 27 April 2023
Published online: 16 May 2023

References

Andoh S, Saito A, Shinagawa H, Ejiri MK (2020) First simulations of day-to-day variability of mid-latitude sporadic E layer structures. Earth Planet Space. https://doi.org/10.1186/s40623-020-01299-8

Andoh S, Saito A, Shinagawa H (2021) Temporal evolution of three-dimensional structures of metal ion layer around Japan simulated by a mid-latitude ionospheric model. J Geophys Res Space Phys 126:e2021JA029267. https://doi.org/10.1029/2021JA029267

Andoh S, Saito A, Shinagawa H (2022) Numerical simulations on day-to-day variations of low-Latitude Es layers at Arecibo. Geophys Res Lett 49(7):e2021GL097473. https://doi.org/10.1029/2021GL097473

Axford WI (1963) The formation and vertical movement of dense ionized layers in the ionosphere due to neutral wind shears. J Geophys Res (1896–1977) 68(3):769–779. https://doi.org/10.1029/JZ068i003p00769

Beynon WJG, Barrett LM, Endean RPJ (1972) Some studies of sporadic E-layer drifts. Philos Trans Royal Soc Lond Ser A Math Phys Sci 271(1217):613–622

Carter L, Forbes J (1999) Global transport and localized layering of metallic ions in the upper atmosphere. Ann Geophys 17:190–209. https://doi.org/10.1007/s00585-999-0190-6

Chimonas G (1971) Enhancement of sporadic E by horizontal transport within the layer. J Geophys Res (1896–1977) 76(19):4578–4586. https://doi.org/10.1029/JA076i019p04578
Christakis N, Haldoupis C, Zhou Q, Meek C (2009) Seasonal variability and descent of mid-latitude sporadic E layers at Arecibo. Ann Geophys 27(3):923–931. https://doi.org/10.5194/angeo-27-923-2009
Hagan ME, Forbes JM (2002) Migrating and nonmigrating diurnal tides in the middle and upper atmosphere excited by tropospheric latent heat release. J Geophys Res Atmos 107(D24):ACL 6-1-ACL 6-15. https://doi.org/10.1029/2001JD001236
Hagan ME, Burrage MD, Forbes JM, Hackney J, Randel WJ, Zhang X (1999) GSWM-98: results for migrating solar tides. J Geophys Res Space Phys 104:6813–6827. https://doi.org/10.1029/1998JA900125
Haldoupis C (2011) A tutorial review on sporadic E layers. In: Abdu MA, Pancheva D (eds) Aeronomy of the earth's atmosphere and ionosphere. Springer, Netherlands, pp 381–394. https://doi.org/10.1007/978-94-007-0326-1_29
Haldoupis C (2012) Midlatitude sporadic E. A typical paradigm of atmosphere-ionosphere coupling. Space Sci Rev 168:1–21. https://doi.org/10.1007/s11214-011-9786-8
Haldoupis C, Pancheva D (2006) Terdiurnal tidelike variability in sporadic E layers. J Geophys Res Space Phys. https://doi.org/10.1029/2005JA011522
Haldoupis C, Meek C, Christakis N, Pancheva D, Bourdillon A (2006) Ionogram height-time-intensity observations of descending sporadic E layers at mid-latitude. J Atmos Sol-Terr Phys 68(3):539–557. https://doi.org/10.1016/j.jastp.2005.03.020
Haldoupis C, Haralambous H, Meek C (2020) On the necessity of using foμEs instead of foEs in estimating the intensity and variability of sporadic E layers. J Atmos Sol-Terr Phys 206(105):327. https://doi.org/10.1016/j.jastp.2020.105327
Huba JD, Krall J, Drob D (2019) Global ionospheric metal ion transport with SAMI3. Geophys Res Lett 46(14):7937–7944
Jacobi C, Arras C, Geißler C, Lilienthal F (2019) Quarterdiurnal signature in sporadic E occurrence rates and comparison with neutral wind shear. Ann Geophys 37(3):273–288. https://doi.org/10.5194/angeo-37-273-2019
Jin H, Miyoshi Y, Fujiwara H, Shinagawa H, Terada K, Terada N, Ishii M, Otsuka Y, Saito A (2011) Vertical connection from the tropospheric activities to the ionospheric longitudinal structure simulated by a new Earth's whole atmosphere-ionosphere coupled model. J Geophys Res Space Phys. https://doi.org/10.1029/2010JA015925
Jin H, Miyoshi Y, Pancheva D, Mukhtarov P, Fujiwara H, Shinagawa H (2012) Response of migrating tides to the stratospheric sudden warming in 2009 and their effects on the ionosphere studied by a whole atmosphere-ionosphere model GAIA with COSMIC and TIMED/SABER observations. J Geophys Res Space Phys 117(10):A10323
Koizumi T (1969) Some characteristics of the Es layer in Japan. J Radio Res Lab 16(17):17–49
Kolawole L, Derblom H (1978) Skywave backscatter studies of temperate latitude Es. J Atmos Terr Phys 40(7):785–792. https://doi.org/10.1016/0021-9169(78)90029-6
Liu HL, McInerney JM, Santos S, Lauritzen PH, Taylor MA, Pedatella NM (2014) Gravity waves simulated by high-resolution whole atmosphere community climate model. Geophys Res Lett 41(24):9106–9112. https://doi.org/10.1002/2014GL062468
Maeda J, Heki K (2014) Two-dimensional observations of midlatitude sporadic E irregularities with a dense GPS array in Japan. Radio Sci 49:28–35. https://doi.org/10.1002/2013RS005295
Maeda J, Heki K (2015) Morphology and dynamics of daytime mid-latitude sporadic-E patches revealed by GPS total electron content observations in Japan. Earth Planet Space. https://doi.org/10.1186/s40623-015-0257-4
Manson A, Meek C, Hagan M, Hall C, Hocking W, MacDougall J, Franke S, Riggin D, Fritts D, Vincent R, Burrage M (1999) Seasonal variations of the semi-diurnal and diurnal tides in the MLT: multi-year MF radar observations from 2 to 70°N, and the GSWM tidal model. J Atmos Sol-Terr Phys 61(11):809–828. https://doi.org/10.1016/S1364-6826(99)00045-0
Mathews JD (1998) Sporadic E: current views and recent progress. J Atmos Sol-Terr Phys 60(4):413–435
Mathews JD, Bekeny FS (1979) Upper atmosphere tides and the vertical motion of ionospheric sporadic layers at Arecibo. J Geophys Res Space Phys 84(A6):2743–2750. https://doi.org/10.1029/JA084iA06p02743
Miyoshi Y, Fujiwara H (2003) Day-to-day variations of migrating diurnal tide simulated by a GCM from the ground surface to the exobase. Geophys Res Lett. https://doi.org/10.1029/2003GL017695
Miyoshi Y, Pancheva D, Mukhtarov P, Jin H, Fujiwara H, Shinagawa H (2017) Excitation mechanism of non-migrating tides. J Atmos Sol-Terr Phys 156:24–36. https://doi.org/10.1016/j.jastp.2017.02.012
Miyoshi Y, Jin H, Fujiwara H, Shinagawa H (2018) Numerical study of traveling ionospheric disturbances generated by an upward propagating gravity wave. J Geophys Res Space Phys 123(3):2141–2155. https://doi.org/10.1002/2017JA025110
Muafiry I, Heki K, Maeda J (2018) 3D tomography of midlatitude sporadic-E in Japan from GNSS-TEC data. Earth Planet Space 70:45. https://doi.org/10.1186/s40623-018-0815-7
Obenberger KS, Dowell J, Fallen CT, Holmes JM, Taylor GB, Varghese SS (2021) Using broadband radio noise from power-lines to map and track dense Es structures. Radio Sci 56(2):e2020RS007169. https://doi.org/10.1029/2020RS007169
Oberheide J, Hagan M, Richmond A, Forbes J (2015) DYNAMICAL METEOROLOGY—atmospheric tides. In: North GR, Pyle J, Zhang F (eds) Encyclopedia of atmospheric sciences. Academic Press, Cambridge, pp 287–297. https://doi.org/10.1016/B978-0-12-382225-3.00409-6
Oikonomou C, Haralambous H, Leontiou T, Tsagouri I, Buresova D, Mošna Z (2022) Intermediate descending layer and sporadic E tidelike variability observed over three mid-latitude ionospheric stations. Adv Space Res 69(1):96–110. https://doi.org/10.1016/j.asr.2021.08.038
Pedatella NM, Liu HL, Hagan ME (2012) Day-to-day migrating and nonmigrating tidal variability due to the six-day planetary wave. J Geophys Res Space Phys. https://doi.org/10.1029/2012JA017581
Picone JM, Hedin AE, Drob DP, Aikin AC (2002) NRLMSISE-00 empirical model of the atmosphere: statistical comparisons and scientific issues. J Geophys Res 107(A12):1468
Raizada S, Smith JA, Lautenbach J, Aponte N, Perillat P, Sulzer M, Mathews JD (2020) New lidar observations of Ca^+ in the mesosphere and lower thermosphere over Arecibo. Geophys Res Lett 47(5):e2020GL087,e2020GL087113. https://doi.org/10.1029/2020GL087113
Rao GL, Rao M (1972) Horizontal drifts in E- and Es-layers for a middle latitude station. J Atmos Terr Phys 34(3):537–541. https://doi.org/10.1016/0021-9169(72)90056-6
Resende LCA, Batista IS, Denardini CM, Carrasco AJ, de Fátima Andrioli V, Moro J, Batista PP, Chen SS (2016) Competition between winds and electric fields in the formation of blanketing sporadic E layers at equatorial regions. Earth Planet Space 68(1):201. https://doi.org/10.1186/s40623-016-0577-z
Solomon SC, Roble RG (2015) Thermosphere. In: North GR, Pyle J, Zhang F (eds) Encyclopedia of atmospheric sciences. Academic Press, Cambridge, pp 402–408. https://doi.org/10.1016/B978-0-12-382225-3.00408-4
Sun W, Zhao X, Hu L, Yang S, Xie H, Chang S, Ning B, Li J, Liu L, Li G (2021) Morphological characteristics of thousand-kilometer-scale Es structures over China. J Geophys Res Space Phys 126(2):e2020JA028712. https://doi.org/10.1029/2020JA028712
Tanaka T (1979) Sky-wave backscatter observations of sporadic-E over Japan. J Atmos Terr Phys 41(2):203–215. https://doi.org/10.1016/0021-9169(79)90013-8
Thébault E, Finlay CC, Beggan CD, Alken P, Aubert J, Barrois O, Bertrand F, Bondar T, Boness A, Brocco L, Canet E, Chambodut A, Chulliat A, Coïsson P, Civet F, Du A, Fournier A, Fratter I, Gillet N, Hamilton B, Hamoudi M, Hulot G, Jager T, Korte M, Kuang W, Lalanne X, Langlais B, Léger JM, Lesur V, Lowes FJ, Macmillan S, Mandea M, Manoj C, Maus S, Olsen N, Petrov V, Ridley V, Rother M, Sabaka TJ, Saturnino D, Schachtschneider R, Sirol O, Tangborn A, Thomson A, TØffner-Clausen L, Vigneron P, Wardinski I, Zvereva T (2015) International geomagnetic reference field: the 12th generation. Earth Planet Space 67:79
Whitehead JD (1961) The formation of the sporadic-E layer in the temperate zones. J Atmos Terr Phys 20(1):49–58
Whitehead JD (1970) Production and prediction of sporadic E. Rev Geophys 8(1):65–144. https://doi.org/10.1029/RG008i001p00065
Whitehead JD (1989) Recent work on mid-latitude and equatorial sporadic-E. J Atmos Terr Phys 51(5):401–424

Wu J, Feng W, Liu HL, Xue X, Marsh DR, Plane JMC (2021) Self-consistent global transport of metallic ions with WACCM-X. Atmos Chem Phys 21(20):15619–15630. https://doi.org/10.5194/acp-21-15619-2021
Yiğit E, Medvedev AS (2017) Influence of parameterized small-scale gravity waves on the migrating diurnal tide in earth's thermosphere. J Geophys Res Space Phys 122(4):4846–4864. https://doi.org/10.1002/2017JA024089

Publisher's Note